Journal of Electroceramics, 9, 137–150, 2002

Annealing and Microstructural Characterization of Tin-Oxide Based Thick Film Resistors

K.M. ANIS RAHMAN,[1,*,†] CHRISTOPHER J. DURNING,[1] SUSAN C. SCHNEIDER,[2] MARTIN A. SEITZ[2] & W.A. CHIOU[3]

[1]*Department of Chemical Engineering and Applied Chemistry, Columbia University, New York, NY 10027, USA*
[2]*Department of Electrical and Computer Engineering, Marquette University, Milwaukee, WI 53233, USA*
[3]*Department of Materials Science and Engineering, Northwestern University, Evanston, IL 60208, USA*

Submitted October 2, 2002; Revised October 2, 2002; Accepted October 17, 2002

Abstract. The sheet resistance of tin oxide based thick-film resistors exhibits two regions of temperature-dependence, described by hopping (23°C–200°C) and diffusion mechanisms (200°C–350°C), respectively. Annealing these samples causes the sheet resistance to increase in both regions. In the post-annealed samples, the hopping conduction range is extended by 50°C (23°C–250°C) while the hopping parameter, T_0, is decreased by more than 50%. The activation energy of diffusion (0.60 eV) is the same for both pre- and post annealed samples, but the magnitude of resistance in the diffusion controlled region is increased significantly as a result of annealing. These changes are explained in terms of a net decrease in the concentration of tin ions in the glass matrix. From a careful microstructural study it was found that a conduction path composed of tin-oxide grains or their clusters in contact with each other does not exist in the present system. HREM micrographs showed the presence of nanocrystalline tin-oxide particles in the glass phase separating the tin-oxide grain clusters. Estimated average separation between the nanocrystals in 4 nm, consistent with a variable-range hopping conduction via the dissolved tin ions in the glass matrix.

Keywords: thick-film resistor, tin-oxide, annealing microstructure, variable-range hopping, ionic diffusion

1. Introduction

Thick-Film Resistors (TFRs) are a class or resistive material used in a variety of applications [1]. These materials are fabricated from an "ink" that is made by mixing a conducting phase and a dielectric phase in known proportions via an organic binder such as ethylcellulose [2]. The ink is applied on an insulating substrate, dried in air and the assembly is then sintered at temperatures well above the glass transition point. The thickness of the finished resistor may vary from a few micrometers to hundreds of micrometers, depending on the type of application. An important parameter that characterizes the TFRs is the sheet resistance [3], $R_\square$, given by $R_\square = Rw/l$, where R is the measured resistance of a resistor with width w and length l. Many different oxides and glasses may be used as the conducting and dielectric phases, respectively, to produce the TFRs.[1] For tin-oxide based TFRs[2] studied by impedance spectroscopy (IS) [4] it was found that the sheet resistance, obtained by analyzing the impedance spectra, exhibits two regions of behavior over a temperature range 23°C–350°C. In region-I (23°C–200°C) conduction was explained satisfactorily by the variable-range hopping [5] mechanism. At higher temperatures (region-II, 200°C to ∼350°C), the observed behavior is consistent with an ion-exchange type diffusion [6], with measured activation energy of 0.60 eV. It is assumed that, in region-I ionic tin dissolved in glass served as the hopping sites, while in region-II, higher temperatures enable these tin ions (Sn^{4+}) to participate in ion-exchange type diffusion

*To whom all correspondence should be addressed.
†Present address: 2218 Southpoint Drive, Hummelstown, PA 17036, USA.

with a network forming cation of the glass matrix, such as, Na^+ [6].

In this paper we investigate the conduction mechanism of tin-oxide based TFRs by impedance spectroscopic measurements. For studying annealing characteristics, time-dependent AC impedance measurements were carried out in-situ as the samples were being annealed at different fixed temperatures. Since the composition of the TFRs contain 70–85% glass, impedance measurements were extended to study the behavior of specimens made from 100% glass as well. A group of TFR samples were annealed and then cooled down to room temperature. The temperature dependence was then studied by a conventional DC method.

We also investigate the microstructure of these TFRs (Section 4). From a physical point of view, the conduction processes are determined mainly by the microstructure. This depends on several factors such as ingredient materials, the thermodynamics of sintering and the sintering conditions i.e., whether solid or liquid phase sintering took place [2]. Electron microscopy was conducted to study the local microstructure of the glass-grain boundary and the glassy regions that separate the grain-cluster regions.

2. Materials and Methods

Tin-oxide based TFRs for the present study were obtained from the Lapp Insulator Company, LeRoy, NY. TFRs of three different compositions designated as L70, L80 and L85 were studied, where L70 stands for a sample containing 70% glass and 30% metal-oxide by weight, and similarly for L80 and L85 samples. The main constituents of glass are SiO_2 (61%), CaO (13%), Al_2O_3 (11%) with small amounts of Na_2O (∼1%), K_2O (∼3%), MgO (∼3%) and ZnO (∼4.5%). The metal-oxide was composed mainly of SnO_2 with a small percentage (∼5%) of Sb_2O_5 mixed in it whose purpose is believed to dope the tin-oxide in-situ [7]. Despite the presence of a small amount of antimony-oxide, these materials are historically known as tin-oxide based glazes [7] or thick film resistors.

The sample geometry, configuration and the impedance measurement setup are identical to those described elsewhere [4] and reproduced in Fig. 1, showing the geometry and electrode attachment scheme. As manufactured, the samples were in the shape of a rod of approximately 1" dia. The rod shaped samples were first cut into disks (∼0.6 cm thick) and then cut into wedge (∼1 cm length) in order to attach electrodes. Ptaninum wires (3 mil dia) were attached to Au-Pd pads that were previously sputter deposited on the resistor surface making sure that the thickness of the resistor material was covered by deposited pad (see Fig. 1). A two-probe electrode configuration was used for both AC and DC measurements.

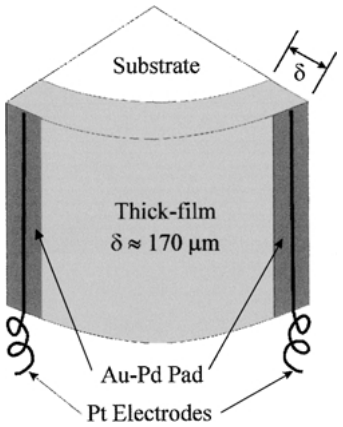

Fig. 1. Sample geometry (not in scale) and electrode arrangement.

To carry out time-dependent AC measurements, the measurement cell was preheated to a given temperature and held at that value until all time-dependent data acquisition were over. Impedance data were acquired continuously at fixed intervals until such time when any changes in the consecutive spectra could not be identified by visual inspection (see Fig. 2). The impedance measurements were repeated at various preset temperatures; for each temperature a new sample was used. Following a similar procedure, measurements were repeated on samples made from 100% glass, designated as Base-Glaze (BG) samples.

At lower temperatures ($<200^\circ$C) the changes in the spectra were slower, therefore, time dependent data were acquired at an interval of an hour. At higher temperatures ($\geq 200^\circ$C), however, the changes in the spectra were much faster, therefore, data were acquired at half an hour intervals. All IS spectra were acquired over a frequency range of 5 Hz to 13 MHz using an automated HP 4192A impedance analyzer; it took about one minute to acquire each individual spectrum over the entire frequency range. At several temperatures, IS spectra were acquired for more than 300 hours. As a result, a huge number of spectra were collected during the time-dependent measurements. These spectra were analyzed by an automated analysis algorithm [8] based

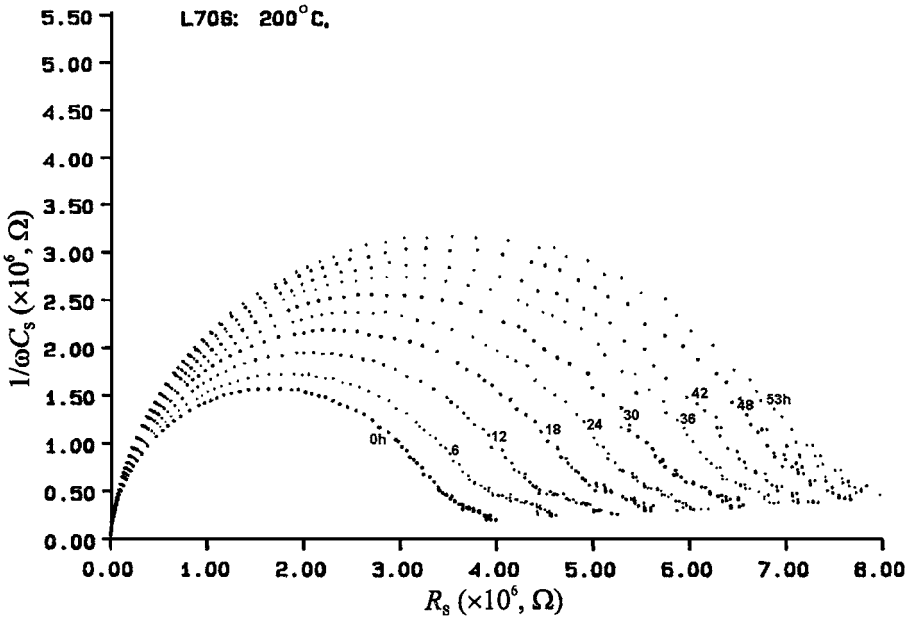

Fig. 2. Time-dependent variation in the impedance spectra of an L70 sample at 200°C.

on Tsai and Whitmore's prescription [9] that accelerated the analysis process significantly. However, this automated algorithm is suitable only for those spectra containing a single prominent relaxation process, as was the case for the present samples.

Specimens for transmission electron microscopy (TEM) were prepared by cutting a small piece of the TFR by a diamond wafering wheel. The TFR piece was cleaned in an ultrasonic bath, dried in air, and then mounted on a metal block with crystalbond, keeping the glaze side in contact with the block. The substrate was removed by polishing on a coarse (200 grit) rotating Buehler polisher. The thickness of the glaze was brought down to about 100 μm by subsequent polishing with finer grits. Further polishing was done on a fine polishing cloth using syton, thereby reducing the sample thickness to about 20 μm. The resulting film was then mounted on a holey Cu grid and finally thinned in an ion-milling machine to electron transparency. TEM specimens were studied using a Hitachi H-700H 200 kV TEM and a Hitachi H-9000 300 kV high resolution TEM. Selected specimens were further examined with a Hitachi HF-2000 cold field emission atomic resolution electron microscope. Energy dispersive X-ray (EDS) spectra were taken from the tin-oxide particles as well as from the inter-cluster glass phase with a beam probe size of approximately 3 nm.

3. Results and Discussion

3.1. Annealing Study

3.1.1. In-situ *IS measurements.* Time dependent variations of the IS spectra of an L70 sample at 200°C are shown in Fig. 2. The spectra acquired for L80 and L85 samples (not shown here) also exhibited a similar pattern and a similar time-dependent changes. It is evident from Fig. 2 that these spectra are predominantly composed of a single semi-circular arc, however, at low frequencies, some scattered data points are present which may appear as an additional relaxation process. Figure 3 exhibits an example of data fitting procedure of a spectrum at $t = 30$ h. The prominent semicircular segment of this spectrum (and subsequently all others) was fitted well by the equivalent circuit shown in Fig. 4. It was found that the depression angle (θ) was negative with very small magnitude ($-5^\circ < \theta < 0^\circ$), indicating a Debye-like relaxation.

We followed the algorithm of Tsai and Whitmore [9] to further analyze the spectra in the low frequency region by subtracting the main equivalent circuit (Fig. 4), leaving only the low-frequency segment as the residuals. In order to qualifying the low frequency segment of the spectra as a "relaxation process," a relaxation-time need to be established. However, using our present

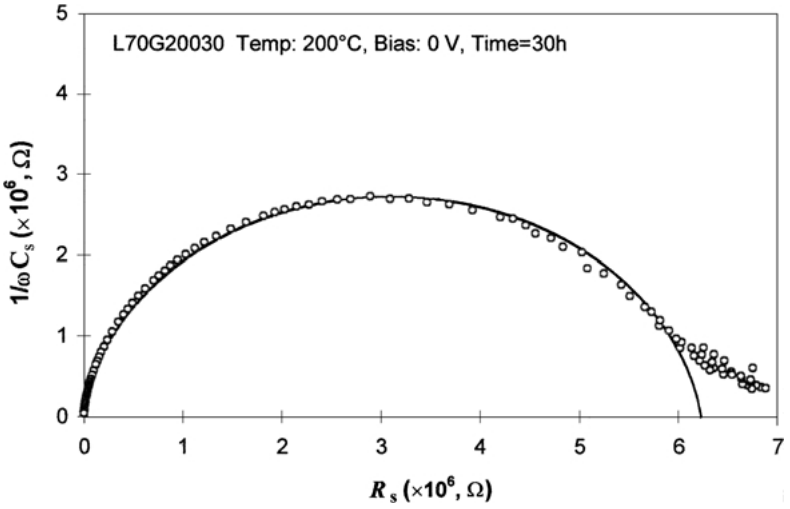

Fig. 3. Example of the fitting process and determination of the equivalent circuit.

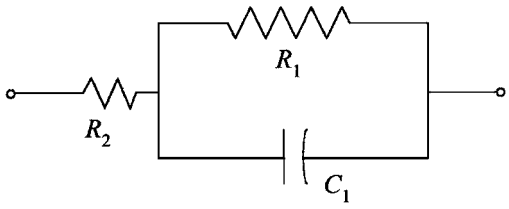

Fig. 4. An equivalent circuit model of the tin oxide based TFR samples.

analysis tool we were not able to do so. For a given spectrum, the analysis procedure subtracts a fitted circuit (e.g., Fig. 4) from the spectrum and then fitting can be continued with the residual data to discover additional sub-circuits. The residual data of the present samples, however, do not exhibit a physically meaningful, clear-cut relaxation process. Therefore, most likely the scattered points in the low frequency region are due to an electrode effect whose origin is not clear at this point.

Similar results were obtained from fitting other spectra acquired in these experiments; therefore, these samples can be represented by the equivalent circuit shown in Fig. 4. Here, the resistance R_2 is assumed to be due to the tin oxide grains; the parallel combination of R_1 and C_1 is assumed to arise from the glassy medium separating the grains. An identical equivalent circuit was also used to describe the room temperature behavior and the temperature dependent behavior [4] of samples with identical compositions. However, while there is no apparent time dependent change in the structure of the equivalent ciruit, its parameters are expected to exhibit time dependent variations as indicated by the spectra in Fig. 2. From the spectra it was found that the resistance R_2 is negligible compared to R_1. From the plots of Figs. 2 and 3 it can be seen that R_2 corresponds to the left intercept and R_1 corresponds to the right intercept of the spectra; hence it can be assumed that $R_2 \ll R_1$. This is also consistent with the assumption that R_2 arises from the tin-oxide grains while the glassy phase separating the grain-clusters give rise to R_1 and C_1.

Figure 5 shows a plot of the normalized resistance, $R_\square(t)/R_\square(t=0)$, obtained by normalizing R_1 at 200°C for an L70 sample. It can be seen from this plot that as t increases, the $R_\square(t)/R_\square(t=0)$ curve grows and then tends to reach saturation. Figure 6 exhibits the time-dependent behavior of base-glaze (BG) samples (made from 100% glass) over the temperature range 200°C–291°C. The normalized resistance of the BG samples does not exhibit any time-dependent changes at a fixed temperature as was observed for the tin-oxide containing TFR samples. Therefore, it may be assumed that the time-dependent changes observed for the TFRs are due primarily to the fact that they contain metal-oxide in their composition.

Figure 7 shows plots of the normalized resistance of L70 samples at different temperatures. It can be seen that, the higher the temperature, the faster the growth of $R_\square(t)/R_\square(t=0)$ and the faster the curve reaches saturation. Similar behavior was also observed for L80 and L85 samples. These data (Fig. 7) were fitted by an

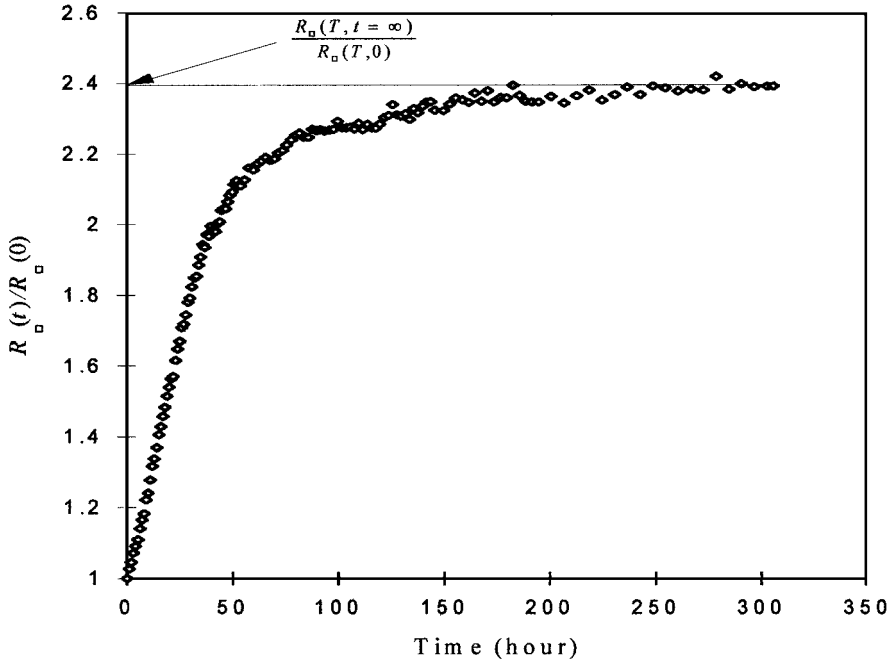

Fig. 5. Normalized resistance, $R_\square(t)/R_\square(t=0)$, computed from R_1 values of L70 samples at 200°C (in air).

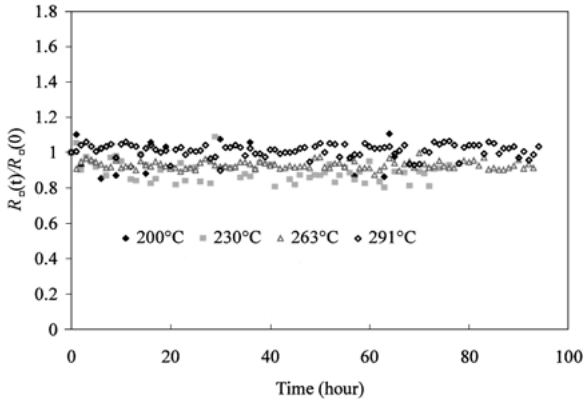

Fig. 6. Normalized resistance, $R_\square(t)/R_\square(t=0)$, computed from R_1 values of Base-Glaze samples at different fixed temperatures (in air).

empirical relation,

$$\left.\frac{R_\square(t)}{R_\square(t=0)}\right|_T = A(T) + B(T)\exp(-t/C(T)) \quad (1)$$

where, $A(T)$ is the saturation value at temperature T (in Kelvin), $B(T) = 1 - A(T)$ and $C(T)$ is the rate constant of growth. It should be emphasized here that Eq. (1) is strictly an empirical relationship without any physical significance assigned to it. The sole use of this equation is to compute the value of $R_\square(t)/R_\square(t=0)$ at saturation ($t = \propto$). The change in resistance at a given temperature, $\Delta R_\square(T)$, was computed from

$$\Delta R_\square(T) = R_\square(t=0) \times \left.\frac{R_\square(t)}{R_\square(0)}\right|_{t=\infty} (\text{Ohms}), \quad (2)$$

where, $R_\square(t=\infty) = A(T)$ obtained from Eq. (1).

Figure 8 shows that the $\Delta R_\square(T)$ data can be fitted quite well up to 250°C by variable-range hopping equation [5, 10–13] expressed as,

$$\Delta R_\square = \Delta R_{\square,0}\exp\left(\frac{T_0}{T}\right)^{1/4}, \quad (3)$$

where, $\Delta R_{\square,0}$ is a constant, and T_0 is the variable-range hopping parameter. Figure 8 indicates that at saturation the resistance exhibits a variable-range hopping mechanism. The variable-range hopping parameter, T_0 can be expressed as [4, 10]

$$T_0 = \frac{(2.587)^4}{N(E_F)R^3 k_B}, \quad (4)$$

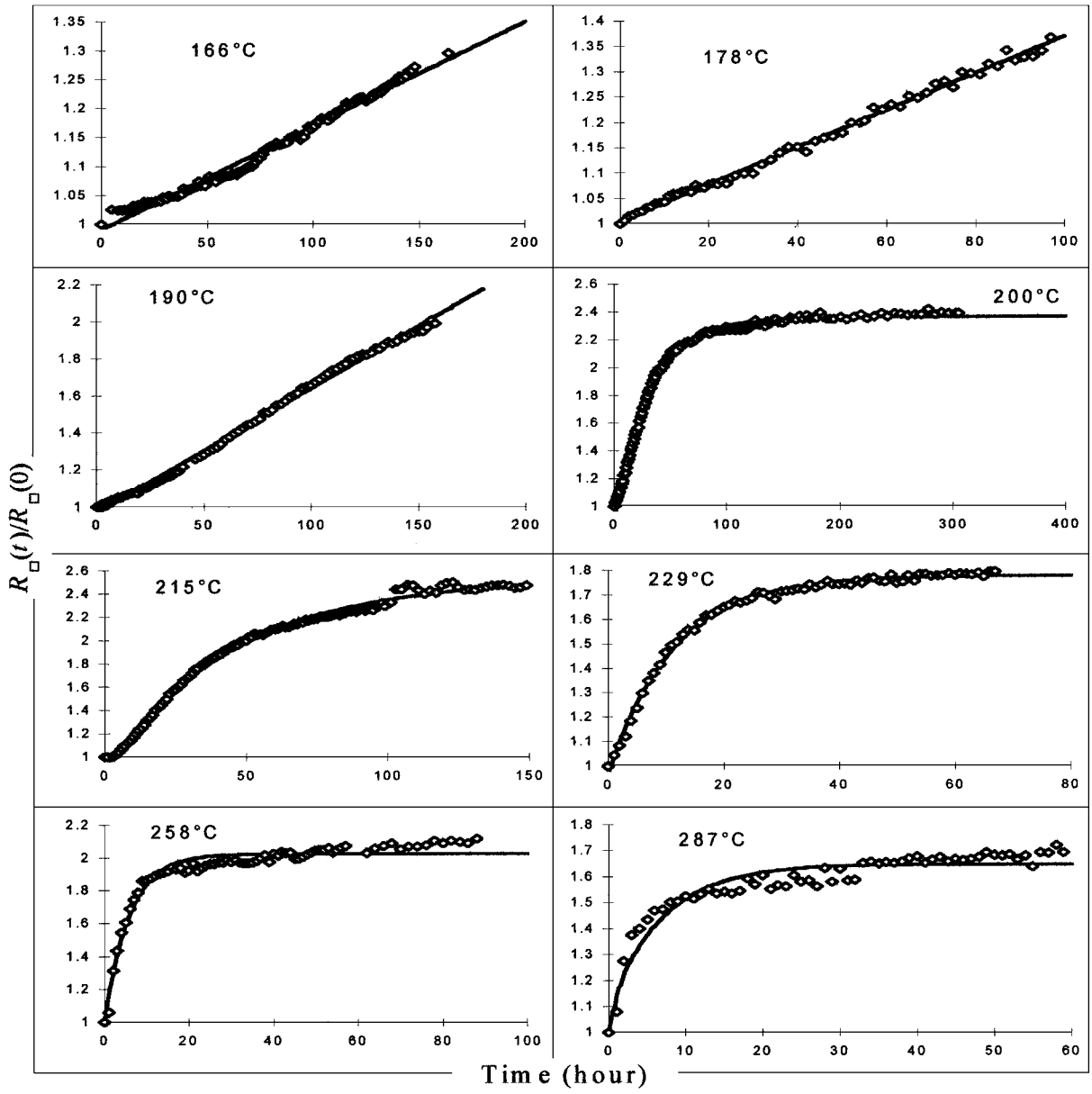

Fig. 7. Normalized resistance, $R_\square(t)/R_\square(t=0)$, computed from R_1 values of L70 samples at different fixed temperatures (in air).

where, $N(E_F)$ is the density of hopping sites, E_F is the Fermi energy, R is the variable-range hopping distance, and k_B is the Boltzmann constant. Equation (4) indicates that a change in the value of T_0 is an indicator of the changes in physical quantities, viz., density of hopping sites, $N(E_F)$, and the hopping distance, R. The values of the variable-range hopping parameter, T_0, for the three different sample compositions of the present study were computed to be,

$$\begin{aligned} T_{0,\mathrm{L70}} &= (1.34 \times 10^7 \pm 0.52 \times 10^5)\ \mathrm{K}, \\ T_{0,\mathrm{L80}} &= (1.61 \times 10^7 \pm 0.64 \times 10^5)\ \mathrm{K}, \\ T_{0,\mathrm{L85}} &= (1.64 \times 10^7 \pm 0.63 \times 10^5)\ \mathrm{K}. \end{aligned} \tag{5}$$

where, the subscripts L70, L80 and L85 indicate the value obtained for the respective group of samples. For

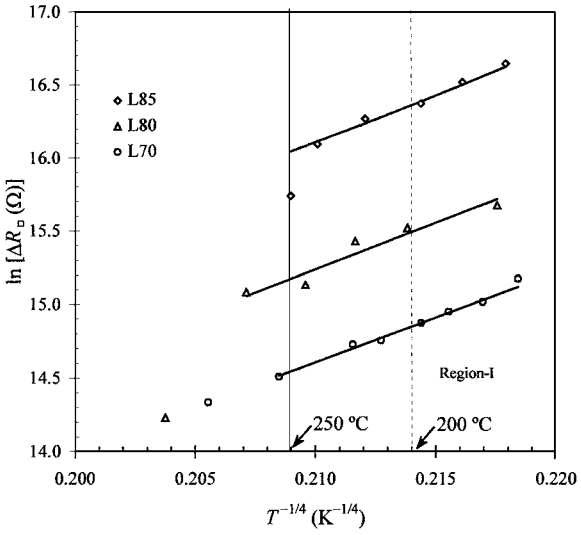

Fig. 8. $T^{-1/4}$ dependence of $\ln(\Delta R_{\square}(T))$. The solid lines are regression lines fitted through respective data set.

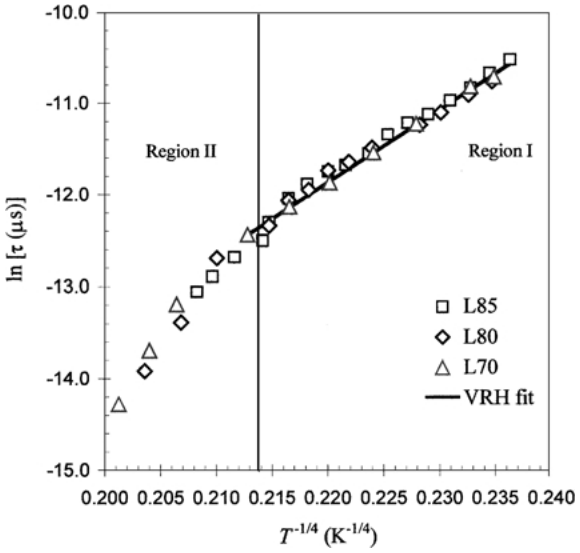

Fig. 9. $T^{-1/4}$ dependence of $\ln(\tau(T))$ shows existence of two temperature dependent regions similar to $R_{\square}$ vs. $T^{-1/4}$ data. The solid line is the VRH fit in region I (see text for explanation of overlapping data points).

pre-annealed samples, the corresponding values were reported before [4], they are:

$$T_{0,\mathrm{L70}} = (2.7 \times 10^7 \pm 4.8 \times 10^5)\ \mathrm{K},$$
$$T_{0,\mathrm{L80}} = (3.2 \times 10^7 \pm 6.6 \times 10^5)\ \mathrm{K}, \qquad (6)$$
$$T_{0,\mathrm{L85}} = (3.9 \times 10^7 \pm 6.2 \times 10^5)\ \mathrm{K}.$$

Comparing the values of T_0s of pre-annealed [4] and post-annealed samples, it can be seen that, the T_0s for the post-annealed samples are between 50–58% of those obtained for the pre-annealed ones. This decrease in the value of T_0 corresponds to an increase in the quantity $N(E_F)R^3$ [Eq. (4)]. The physical significance of this change is discussed below.

3.1.2. Post-annealed DC measurements. The annealing experiments were augmented by DC measurements with a view to probe further the nature of changes due to annealing. The temperature dependence of the relaxation time, $\tau(T)$ of these samples was reported earlier [4]; where it was found that $\tau(T)$ follows the trend of the resistance, $R_1(T)$, while the temperature dependent change in the capacitive parameter, $C_1(T)$ (see Fig. 4) was negligible. Figure 9 shows a plot of $\ln(\tau)$ as a function of $T^{-1/4}$, where presence of two temperature dependent regions can be seen. Region I can be fitted well by $T^{-1/4}$ law, indicating a variable hopping conduction in this region. It is also evident from Fig. 9 that $\tau(T)$ of all three compositions overlaps. This is because the relaxation time is independent on the geometry of the specimens: $\tau = R_1 C_1 = \rho\varepsilon$.

It was also found that the time dependence of the normalized relaxation time, $\tau(t)/\tau(t=0)$ follows exactly the same trend as the time dependence of the resistance, $R_{\square}(t)/R_{\square}(t=0)$ (Fig. 7), while no appreciable time dependent change was observed in the normalized capacitance, $C_1(t)/C_1(t=0)$. Therefore, a study of changes in resistance alone is expected to suffice to probe the changes that occurred in the specimen as a result of annealing.

Samples from each composition were annealed in excess of 150 hours at a temperature between 275°C–300°C. The duration and temperature for annealing were chosen so that the time-dependent changes in resistance of each sample would reach saturation. The annealed samples were cooled to room temperature and the resistance was then meausured as a function of increasing temperature by a conventional two-probe DC method.

3.2. *Comparison Between the Pre- and Post-annealed Samples*

3.2.1. Hopping conduction in region-I. Figure 10 shows a plot of the post-annealed $R_{\square,\mathrm{dc}}(T)$ data

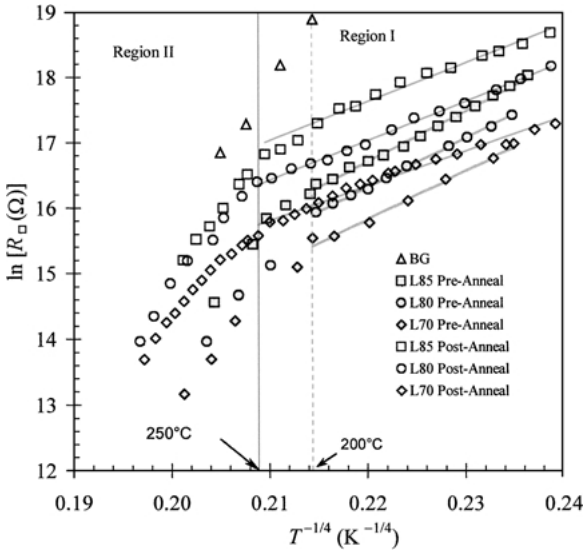

Fig. 10. Plot of ln $R_\square$ vs. $T^{-1/4}$ of pre-annealed and post-annealed samples along with the fitted lines in region-I.

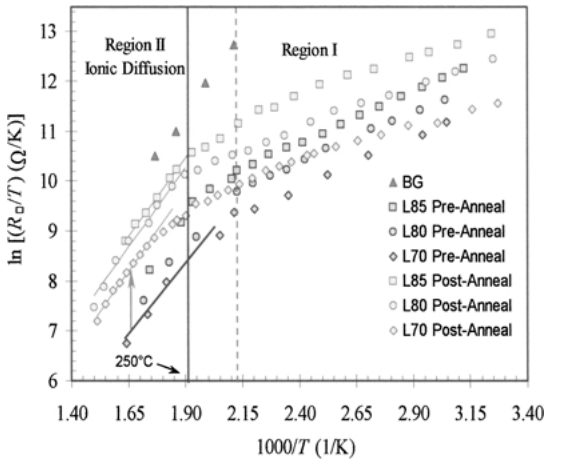

Fig. 11. A plot of post-annealed $\ln R_\square/T$ vs. $1/T$ yields an activation energy of 0.60 eV in region-II. Pre-annealed data are also shown. The up arrow in region II indicates the increase in resistance of L70 samples.

obtained from the DC measurements along with the pre-annealed $R_\square(T)$ data [4]. It can be seen from Fig. 10 that, like $R_\square(T)$, the $R_{\square,\mathrm{dc}}(T)$ data also exhibit two regions of temperature dependence, however, the temperature range of region-I behavior in the post-annealed data has been extended by approximately 50°C, i.e., form room temperature to ∼250°C compared to the pre-annealed case where region-I spanned from room temperature to ∼200°C. The resistance values of the post-annealed samples are increasingly higher than the corresponding pre-annealed values in this region. The values of the variable-range hopping parameters, T_0', in region-I of post-annealed samples from the DC measurements were,

$$\begin{aligned} T'_{0,\mathrm{L70}} &= (8.02 \times 10^6 \pm 0.12 \times 10^5)\ \mathrm{K}, \\ T'_{0,\mathrm{L80}} &= (1.05 \times 10^7 \pm 0.51 \times 10^5)\ \mathrm{K}, \\ T'_{0,\mathrm{L85}} &= (1.24 \times 10^7 \pm 0.47 \times 10^5)\ \mathrm{K}. \end{aligned} \tag{7}$$

Comparing Eq. (7) to Eq. (6), it can be seen that the variable-range hopping parameters of post-annealed samples are between 67–70% of the corresponding numbers obtained for pre-annealed samples. Thus it is seen that the net effect of annealing is always to decrease the value of the variable-range hopping parameter, T_0. The observed decrease in T_0, however, is not always the same. Compared to the pre-annealed case [4] (Eq. (6)), the numbers in Eq. (5) are about 50% while in Eq. (7) they are about 68%. This discrepancy may arise due to the fact that, in the two cases, measurements were done under different conditions: the AC measurements (Eq. (5)) were carried out in-situ, while the DC measurements (Eq. (7)) were done ex-situ.

3.2.2. Ionic diffusion in region-II. Figure 11 shows a plot of $\ln(R_{\square,\mathrm{dc}}/T)$ vs. $1/T$ of the post-annealed measurements along with the $R_\square/T$ data of the pre-annealed samples. An activation energy of 0.60 eV was computed in region-II of post-annealed data; this activation energy is identical to the value obtained in region-II of pre-annealed data. This indicates that the same conduction mechanism is active in region-II of both pre- and post-annealed samples. Conduction in this region is assumed to be due to an ion-exchange (mutual) diffusion [6] of Sn^{4+} with a network forming cation of the glass matrix, such as, Na^+. The basis of this assumption is that a direct diffusion of the Sn^{4+} ions requires much higher activation energy, of the order of 9 eV or more [11]. The observed low activation energy (0.6 eV in region II) in the present case is consistent with reported ion exchange type diffusion of Sn^{4+} with an activation energy of 0.61 eV as determined by electron microprobe analysis in a similar system [6].

Although the activation energy did not change in region-II of the post annealed samples, the resistance values have increased approximately to 3 times the pre-annealed values. In this region the temperature

dependence of the sheet-resistance is described by [4, 12]

$$R_{\square} = R'_{\square,0} T \exp(E_D / k_B T), \tag{8}$$

where, the pre-factor $R'_{\square,0}$ is given by [14]

$$R'_{\square,0} = \frac{k_B T}{n q^2 d^2 \alpha' \nu_0}. \tag{9}$$

Here n is the concentration of the ionic species, q is the total charge per ion, d is the jump distance, α' is a geometrical factor, and ν_0 is the characteristic vibrational frequency. Since annealing did not affect the activation energy, E_D [Eq. (8)], the observed increase in resistance in region-II must be due to an increase in the pre-factor, $R'_{\square,0}$ which is inversely proportional to the concentration of the ionic species, n (Eq. (9)), participating in the diffusion process, that is, $R'_{\square,0} \propto T/n$. Therefore, the observed increase in resistance can be assigned to a decrease in the concentration of the diffusing ionic species, Sn^{4+}. Here, it is thought that the glassy regions in between the tin-oxide clusters were saturated with excess tin during liquid phase sintering of the samples. These excess tin ions could precipitate out during annealing, thereby reducing the concentration of Sn^{4+} in the glass matrix. However, experimental determination of tin-ion concentration was not possible by available means.

In region-I, the variable-range hopping parameter, T_0, is inversely proportional to the factor $N(E_F)R^3$ (Eq. (4)). Therefore, the observed decrease in the value of T_0 (Eqs. (5) and (7)) corresponds to an increase in this product. While it is difficult to discern between relative contributions of these two parameters, $N(E_F)$ and R, it can be surmised that a decrease in the concentration of Sn^{4+} would result in a decrease in the number of hopping sites, $N(E_F)$, which in turn would result in an increase [5] in the hopping distance, R. Therefore, although the first order term $N(E_F)$ in the factor $N(E_F)R^3$ is decreased, an increase in R would have a three-fold effect resulting in a net increase of the factor $N(E_F)R^3$, thus lowering the value of T_0. Indeed this is observed in region-I of the post-annealed data.

3.3. Solubility of Tin and Antimony in Glass-Matrix

For hopping conduction to occur, a finite density of intermediate states [3] is needed in the glassy phase separating the SnO_2 grain clusters. Multivalent tin ions are suitable to serve as the hopping centers because they have the ability to receive and release electrons by changing their valence state. The major constituent of the present TFRs is glass, for instance, L70 samples contains 70% glass. On the other hand, the major constituents of the glass are SiO_2(61%), CaO (13%) and Al_2O_3 (11%).

Conducting a search in the contemporary phase diagram databases, we were not able to find an appropriate phase diagram for the $SiO_2-Sb_2O_5$ system, however, the phase diagram for Si-Sb indicates that Sb would not dissolve in a *Si* lattice at the sintering temperature of the present system. Thus, we assume that Sb is not expected in the glass matrix.

The phase diagram of the SnO-SiO_2 system has been reported in the literature [13]. Nover and Williamson [14] reported on the effects of heat treatment in air on the crystallization and decomposition of SnO-SiO_2 glasses. At temperatures between 550°C and 650°C such glass produced a metastable crystalline phase, $SnSiO_3$. When heated to about 700°C, this phase decomposed to give SnO and SiO_2, and at higher temperatures (>700°C) it decomposed into Sn, SnO_2 and SiO_2. Since the present TFR system was sintered at about 1200°C, the above report [15] supports the assumption that a finite number of tin ions were isolated from the parent oxide, which, upon cooling the samples, would be left localized in the glass matrix and later form nanoparticles of SnO_2 upon further cooling. This finite number of tin ions would form the hopping sites in the glass phase separating the tin-oxide clusters. While it was not possible to estimate the exact number of dissolved tin ions because of the limitations of the available techniques, nonetheless, it can reasonably be assumed that a hopping path, assisted by the multivalent tin ions, can be formed in the present TFR system. Such a conduction path is also consistent with the variable-range hopping mechanism [3] as evidenced by the $T^{-1/4}$ behavior of the resistence. As will be discussed in the next section, such a path is also consistent with the observed microstructure of these samples.

4. Microstructural Investigation

Electron microscopy investigations were conducted to study the microstructure of these TFRs. In particular, SEM was used to look at the overall morphology of the TFRs, while high resolution TEM was used to

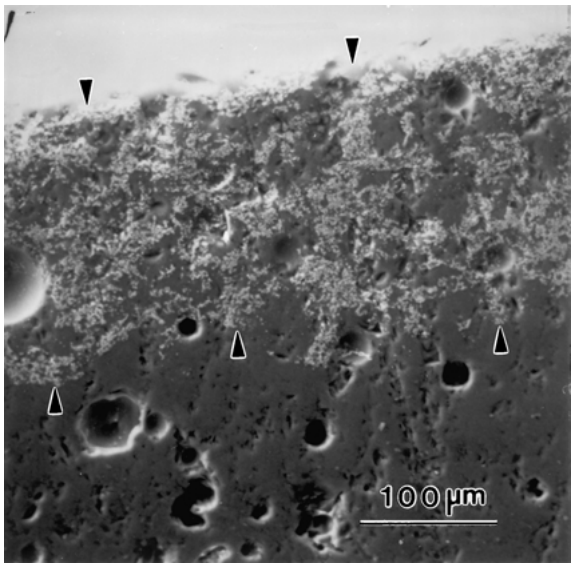

Fig. 12. An SEM micrograph of the glaze-substrate interface of the tin-oxide based TFR samples.

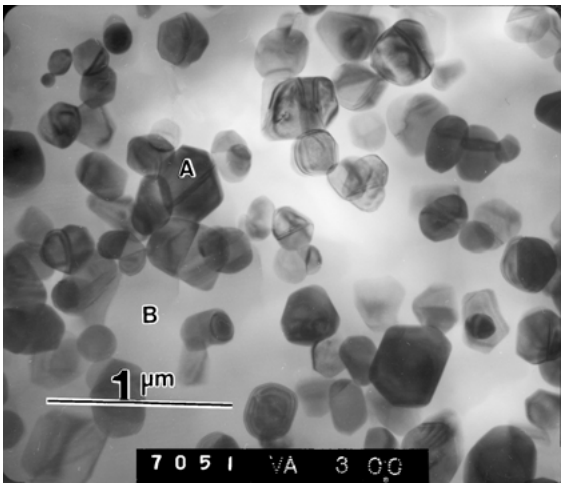

Fig. 13. TEM micrograph showing that tin oxide grain clusters are embedded in the glass matrix.

investigate the local microstructure of the grain boundaries and the grain-glass interfaces. Figure 12 shows an SEM micrograph of the glaze-substrate interface; the glaze side is shown at the top. This micrograph shows an overall arrangement of the tin-oxide grains, formed due to recrystallization after liquid phase sintering (see below), in the glass matrix. A zigzag demarcation line can be observed between the glaze and the porcelain substrate. It also shows that the clusters of tin-oxide grains (white specks) are randomly distributed throughtout the thickness of the glaze and the clusters are separated by glassy layers of varying thicknesses. An average thickness of the glaze was estimated to be 170 μm.

Figure 13 shows a representative TEM micrograph of the glaze area from which it can be seen that the tin oxide grains are embedded in the glassy matrix. From this and other TEM micrographs it was found that the grain size varies between 0.1 μm and 0.8 μm, with an estimated average size of (0.36 ± 0.10) μm. Since these samples were fired at about 1200°C, liquid phase sintering is expected to have occurred. Upon cooling, the tin-oxide is expected to precipitate out and recrystallize. This is indeed evident from the micrograph of Fig. 13. The smooth crystal faces of the SnO_2 grains (as opposed to the sharp cornered particles that usually results from grinding) indicate the precipitation and grain formation of tin-oxide during post-sinter cooling. It can also be seen that the tin-oxide grains form clusters that are embeded in the glassy matrix, and glassy regions separate the clusters from one another. An average thickness of the glass layers separating the tin-oxide grain clusters was estimated to be 0.4 μm. Since typical tunneling distance is of the order of 20 Å [16] or less, a bigger intercluster separation indicates that tunneling conduction is not likely to occur in this system.

High resolution TEM was carried out to examine (i) the interface between tin-oxide grains and glass to see any possible structural changes that might have occurred in the vicinity of the tin-oxide grains by the reaction with glass ingredients during sintering, (ii) the interfaces between tin-oxide grains in a cluster, and (iii) the local microstructure of the glass region separating the tin-oxide cluster. Figure 14 shows a typical interface between the SnO_2 crystalline phase (identified by the lattice fringes) and the amorphous glass phase. The absence of a sharp boundary at the interface can be observed, however, existence of any additional phase at the grain-glass interface is not evident except that the lattice fringes of SnO_2 extend into the glass for about 1 nm.

A lattice image of the grain boundary between two SnO_2 grains is shown in Fig. 15. This micrograph depicts two grains that have joined together at the lattice level, thus indicating the existence of a continuous path within the clusters. If the majority of the grains in a cluster are joined together at the lattice level, then the intracluster conduction would have a lesser or negligible

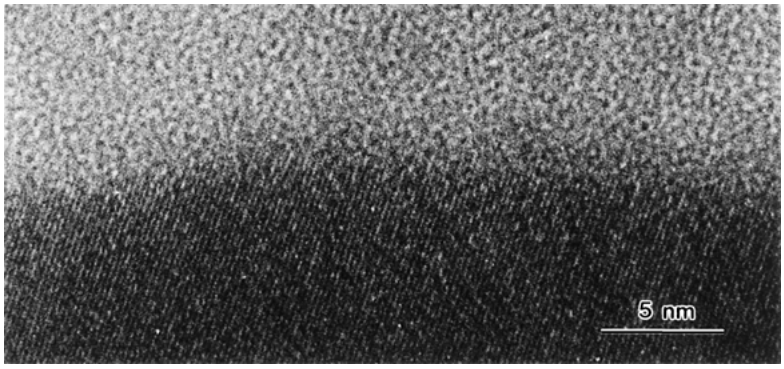

Fig. 14. High resolution micrograph of interface between a tin oxide grain and glass phase.

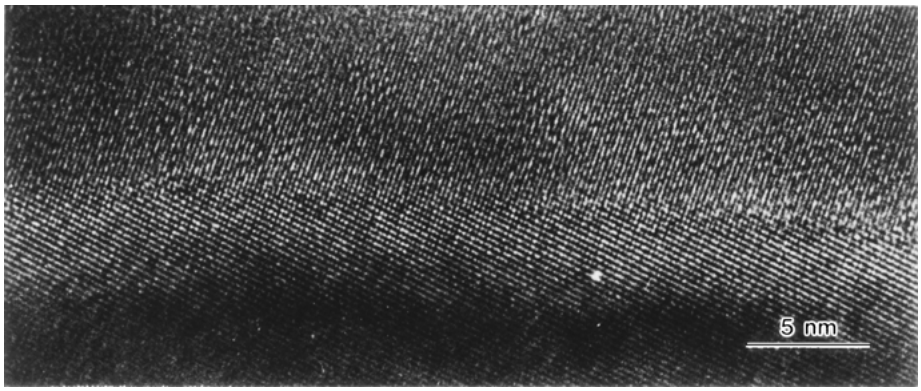

Fig. 15. Lattice image showing the interface between two tin oxide grains.

electrical impedence compared to the conduction path composed of glassy phase between the tin-oxide clusters. This was indeed observed from the impedance spectra (Fig. 2); the value of R_2 was negligible compared to R_1 (Fig. 4), consequently, the glassy region separating the tin-oxide clusters is expected to play the most important role in determining the conduction mechanism.

Figure 16 exhibits a high-resolution micrograph of the glass phase separating the tin-oxide grain clusters. The lattice fringes on the left are due to a tin-oxide grain, while the amorphous glass phase does not exhibit any regular fringe pattern. However, it can be seen that there are small crystallites (a few are indicated by the arrow-heads) of dimension varying between 1 to 2 nm, scattered in the glass phase. These nanocrystalline particles reflect some sort of structural inhomogeneities introduced in the glass matrix [15]. It was suspected that these nanocrystals could form a continuous path in the glass phase that separates the tin-oxide clusters. However, from a careful examination of the high-resolution micrographs, no evidence of a continuous path was found. An average distance between the nanocrystals was estimated to be 4 nm. Since typical tunneling distance is expected to be 1–2 nm [16], therefore, a tunneling path is most likely not present between the clusters via these nanocrystals. Thus a conduction path through the microstructure of the present TFRs would inevitably involve the inter-cluster glass phase.

The inter-planar distance the nanocrystal lattice fringes (Fig. 16) matched with certain d-spacings of SnO_2, e.g., $\langle 112 \rangle$, $\langle 202 \rangle$ and $\langle 220 \rangle$ [17]. Thus it may be assumed that at the firing temperature of about 1200°C the glass matrix was saturated with tin ions; during rapid cooling after the furnace was shut off, tin-oxide has precipitated out to form the grains and the clusters. However, the excess tin, that was not used up by the grain formation process, have formed the nanocrystals during the slow cooling process, long after the furnace was shut off.

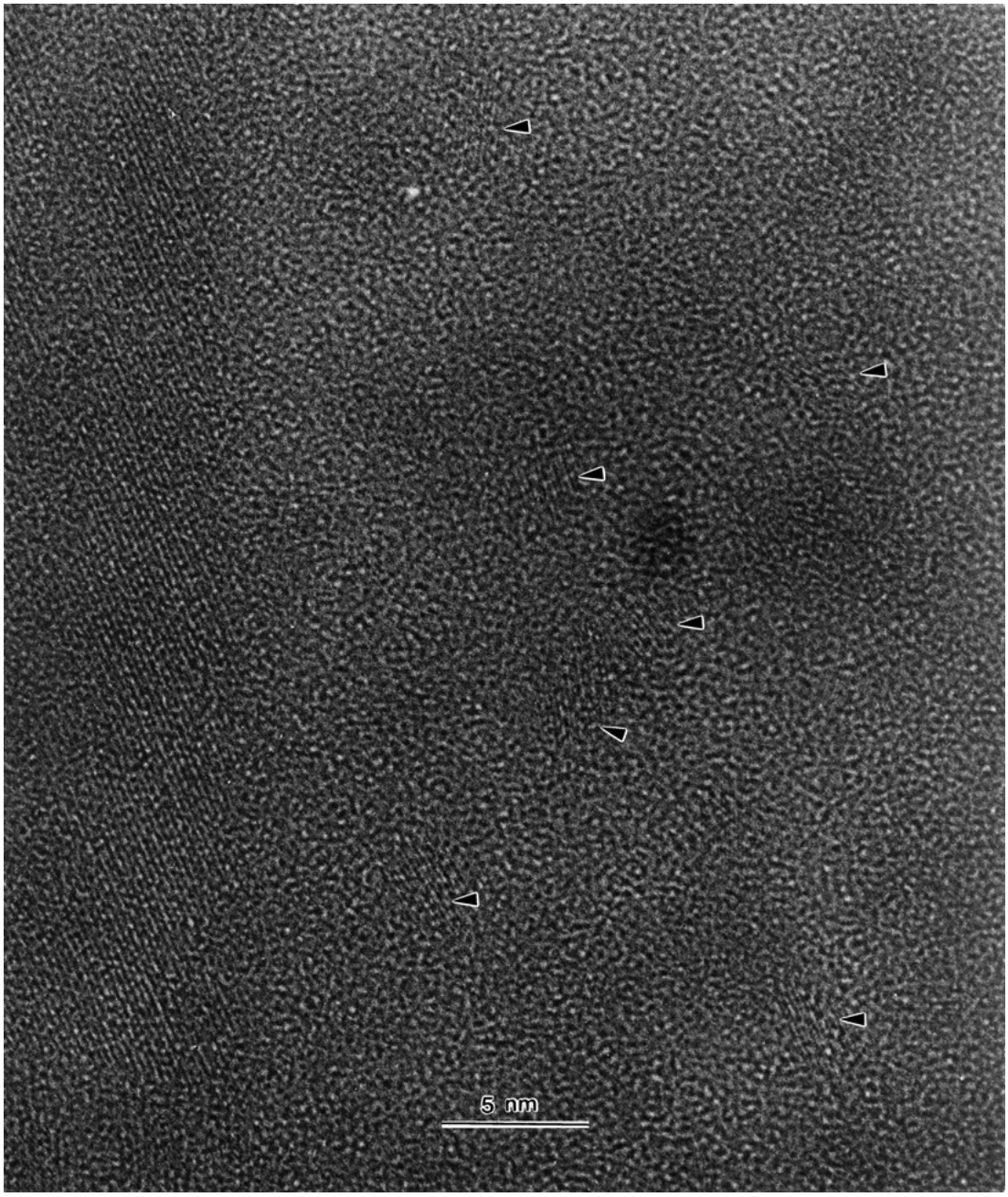

Fig. 16. A lattice image of the glass phase separating the grains. The grain lattice (on the left) is identified by the fringes. The inter-cluster glass phase (on the right) shows presence of nano-crystalline particles (few identified by the arrow-heads).

We acquired EDS spectra (Fig. 17) from a tin-oxide grain and glass regions of the TFR, respectively. EDS analysis of the grain region (marked A in Fig. 13) shows a clear abundance of Sn (Fig. 17(a)) while in the glass matrix area (marked B in Fig. 13) the major component is Si. Thus, it is clearly seen that the grains are composed predominantly of Sn while the glass matrix exhibit an abundance of Si. This is consistent with the ingredients used to fabricate these samples. However, while from the foregoing analysis it can reasonably be

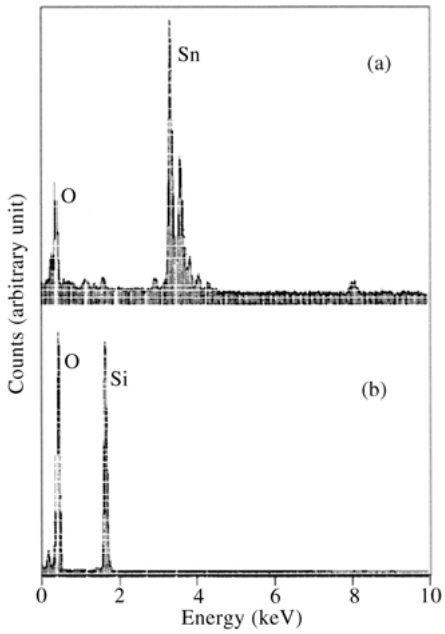

Fig. 17. (a) An EDS spectrum obtained from the grain region (marked A in Fig. 12) showing an abundance of Sn, and (b) a spectrum obtained from the glass matrix region (marked B in Fig. 12) showing an abundance of Si.

assumed that a finite concentration of tin ion has been incorporated in glass due to liquid phase sintering, we were not able to quantify tin ion concentration by the present analysis.

Inspecting Fig. 13 it can also be seen that a conduction path composed solely of the tin-oxide grains and/or their clusters in contact with each other does not exist in the present system. It has been reported that in RuO_2 based TFRs [2, 18–20], a path composed of metal-oxide grains separated by very thin layer of glass serves as the main conduction path via a tunneling mechanism. As an evidence of this proposition, a TEM study by Chiang et al. [20] indicated that the glassy layers separating the RuO_2 grains were only 10–13 Å thick, a distance quite consistent with tunneling mechanism. In the present tin-oxide based TFRs, however, it can be seen that the clusters of SnO_2 grains are separated by much thicker regions of glass ($\sim$0.4 μm) and the nanocrystals within these regions have an average separation of 4 nm.

This large separation is inconsistent with direct tunneling of charge carriers between the clusters but is consistent with hopping mechanism via tin ions serving as hopping sites. According to Mott and Davis [21], Elliot [22] and Sklovskii and Efros [10] a possible mechanism for charge transfer through an amorphous glass is electron hopping between localized states. Morgan et al. [7] And Dyshel' et al. [23, 24] have pointed out that for high resistivity ($\rho > 200$ Ωm) tin-oxide based thick-films, electron hopping may occur via the localized states present in the glass matrix. The present system ($\rho \geq 1900$ Ωm for L70 samples) supports this hypothesis of electron hopping from one tin-oxide cluster to another where tin ions in the glassy layers serve as hopping centers.

5. Conclusions

The annealing behavior in the tin oxide based TFR's of the present study can be described in terms of variable-range hopping and an ion exchange type diffusion, respectively, in the two temperature-dependent regions of interest. The observed increase in the sheet-resistance as a result of annealing is due to a net decrease in the concentration of tin ions in the glass matrix. Based on the results of TEM analysis, it can be concluded that a tunneling path is highly unlikely through the microstructure of the present tin-oxide based TFRs. Electron hopping, assisted by the localized, multivalent tin ions dissolved in the glass during sintering, constitutes the main conduction-path. The hopping path is consistent with Motts $T^{-1/4}$ temperature dependence of the resistance.

Notes

1. It may be noted here that resistor inks comonly used in hybrid microelectronic circuits are made from RuO_2 and are also called thick film resistor. However, RuO_2 based TFRs are significantly different from the ones being considered here; they differ in composition, in type of glass used as well as in processing. For this reason, one should not draw a direct comparison between these two classes of TFRs.
2. Although the actual composition of the tin-oxide based TFRs contain small amount of antimony oxide, historically these materials are refered to as tin-oxide based glaze or TFR.

References

1. J.E. Sergent and C.A. Harper (ed.), *Hybrid Microelectronics Handbook*, 2nd edn. (McGraw-Hill, New York, 1995); M.L. Topfer, *Thick-Film Microelectronics, Fabrication, Design and Applications* (Van Nostrand Reinhold, New York, 1971); M. Prudenziati (ed.), *Thick Film Sensors* (Elsevier, New York,

1994); M. Pecht (ed.), *Integrated Circuit, Hybrid, and Multichip Module Package Design Guidelines: A Focus on Reliability* (Wiley, New York, 1994); J.A. King (ed.), *Materials Handbook for Hybrid Microelectronics* (Artech House, Boston, 1988); B.V. Hiremath (ed.), *Ceramic Thin and Thick Films*, Ceramic Transactions; Vol. 11 (American Ceramic Society, Westerville, OH, 1990).
2. R.W. Vest, "Conduction mechanisms in thick film microcircuits," Technical Report, Purdue University, 1975.
3. L.I. Maissel, in *Handbook of Thin Film Technology*, edited by L.I. Meissel and R. Glang (McGraw-Hill, New York, 1983), ch. 13.
4. K.M. Anisur Rahman, S.C. Schneider, and M.A. Seitz, *Journal of the American Ceramic Society*, **80**(5), 1198 (1997).
5. N.F. Mott, *Conduction in Non-Crystalline Materials*, 2nd edn. (Clarendon Press, Oxford, 1987).
6. A.S. Sanyal and J. Mukerji, *Physics Chem. Glasses*, **24**(4), 79 (1983).
7. P.M. Morgan, J. Robertson, and R.H. Taylor, *J. Non-Cryst. Solids*, **31**, 367 (1979).
8. K.M. Anisur Rahman, Ph.D. Thesis, Marquette University, Milwaukee, WI, 1994.
9. Y.T. Tsai and D.H. Whitmore, *Solid State Ionics*, **7**, 129 (1982).
10. B.I. Shklovskii and A.L. Efros, *Electronic Properties of Doped Semiconductors* (Springer-Verlag, Berlin, 1984).
11. R.H. Taylor, J. Robertson, S.B. Morris, J. Williamson, and A. Atkinson, *J. Mater. Sci.*, **15**, 670 (1980).
12. H.L. Tuller, D.P. Button, and D.R. Uhlmann, *J. Non-Cryst. Solids*, **40**, 93 (1980).
13. E.M. Levin and H.F. McMurdie, *Phase Diagrams for Ceramists 1975 Suppliment* (American Ceramic Society, Ohio, 1975), p. 126K.
14. J. Carbo Nover and J. Williamson, *Phys. Chem. Glasses*, **8**(4), 166 (1967).
15. K. Adachi, S. Iida, J. Ishigame, and S. Sekihara, *J. Mater. Res.*, **6**(8), 1729 (1991).
16. C. Kittel, *Introduction to Solid State Physics*, 5th edn. (John Willey & Sons, New York, 1976), p. 388.
17. Powder Diffraction File. Inorganic volume., Swarthmore, Pa.: Committee on Powder Diffraction Standards, Microfiche No. 1–35 (SCI. MFL/H-117), 1974–1984.
18. G.E. Pike and G.H. Seager, *J. Appl. Phys.*, **48**, 5152 (1977).
19. M. Prudenziati, A. Rizzi, P. Davoli, and A. Mattei, *Il Nuovo Cimento*, **2**, 697 (1983).
20. Y.-M. Chiang, L.A. Silverman, R.H. French, and R.M. Cannon, *J. Am. Ceram. Soc.*, **77**(5), 1143 (1994).
21. A. Davis and N.F. Mott, *Philosophical Magazine*, **22**, 903 (1970).
22. S.R. Elliott, *Philosophical Mag.*, **36**(6), 1291 (1977).
23. D.E. Dyshel', B.M. Rud', and M.D. Smolin, *Sov. Powder Metall. Met. Ceram.*, **26**(11), 920 (1988).
24. D.E. Dyshel', B.M. Rud', M.D. Smolin, and I.A. Stoyanov, *Soviet Journal of Communications Technology & Electronics*, **34**, 145 (1989).